Diels–Alder reactivity of allenylboronic acid pinacol ester and related dienophiles: mechanistic studies and distortion/interaction-activation strain model analysis

Natalia Labadie and Silvina C. Pellegrinet*

Instituto de Química Rosario (CONICET), Facultad de Ciencias Bioquímicas y Farmacéuticas, Universidad Nacional de Rosario, Suipacha 531, Rosario (2000), Argentina

Supporting Information

List of contents:

Computational Methods

All DFT calculations were performed with the Gaussian09 suite of programs.[1] 3D images of optimized structures were generated with CYLview.[2] Multiwfn[3] was used to perform EDA-NOCV calculations and NOCV deformation densities as well as FMOs were visualized with VMD.[4,5] Conformational searches for the reactants, the transitions structures (TSs), and the products were performed to locate the global minima. Initially, a large number of geometries were generated using the conformational search module of Hyperchem with the MM+ method.[6] Full optimization of all selected structures for the concerted mechanisms were then carried out using the hybrid meta-GGA M06-2X functional[7] in conjuction with the 6-31+G* basis set. The M06-2X functional has been found to yield relatively accurate free energies of cycloaddition reactions.[8,9] Additionally, solvent effects in toluene ($\varepsilon = 2.3741$) for the most stable geometries of reagents, TSs, and products were taken into account through full optimizations using the SMD continuum solvation method.[10] This level is denoted SMD(toluene)-M06-2X/6-31+G*. Geometries for all structures were fully optimized and normal mode analysis was used to confirm the nature of the stationary points and to evaluate the thermochemical properties. Reported thermochemical properties include zero-point energies (ZPEs) without scaling and were calculated at 1 atm and 298.15 K, unless otherwise noted. Energy refinements were performed through single point calculations on the optimized geometries using the triple-ζ basis set 6-311++G** including solvent effects (denoted as SMD(toluene)-M06-2X/6-311++G**//SMD(toluene)-M06-2X/6-31+G*). Population analyses were performed to calculate the molecular orbitals of the reactants and analyze the frontier orbital interactions. Intrinsic reaction coordinate (IRCs) calculations were run to verify the connectivity between reactants, TSs and products. To examine the more important interactions in the TSs, we performed natural bond orbital calculations.

For the stepwise radical mechanism, optimization and frequency calculations for minima and TSs were carried out using the unrestricted B3LYP[11,12]/6-31G* method in the gas phase with the "guess = (mix, always)" option to break the orbital symmetry and avoid convergence to closed-shell structures. Initial geometries for all structures were obtained by modifying the optimized geometries of the reactions between **4a** and **2**, reported in our previous work. In all cases, the stability of the wavefunction was checked by running stability calculations on the optimized geometry. Population analyses were performed to obtain atomic spin densities and confirm localization of unpaired electrons.

Conceptual DFT

The global[13] and local[14] reactivity indices, as well as the frontier molecular orbitals (FMOs), for the reactants were calculated. The global electrophilicity index ω has been given by the following

expression, $\omega = \mu^2/2\eta$ (eV), in terms of the electronic chemical potential μ and the chemical hardness η. Both quantities may be approximated in terms of the one-electron energies of the frontier molecular orbitals HOMO and LUMO, $\mu \approx (E_{HOMO} + E_{LUMO})/2$ and $\eta \approx (E_{LUMO} - E_{HOMO})$, respectively. The global nucleophilicity index, N, was computed relative to tetracyanoethylene (TCNE) as $N = E_{HOMO} - E_{HOMO(TCNE)}$ (eV). The maximum charge transfer towards the electrophiles ΔN_{max} were calculated by the equation $-\mu/\eta$. The local nucleophilicity indices, N_k, were computed according to the following expression: $N_k = N.P^-_k$, where P^-_k is the nucleophilic Parr function of atom k, computed using the Mulliken atomic spin density (ASD) by unrestricted single-point of the radical cation resulting from subtracting one electron to the optimized neutral geometry. The local electrophilicity indices, ω_k, were computed according to the following expression: $\omega_k = \omega.P^+_k$, where P^+_k is the electrophilic Parr function of atom k, computed using the Mulliken ASD by unrestricted single-point of the radical anion resulting from adding one electron to the optimized neutral geometry.

Distortion/Interaction-Activation Strain Model Analysis

In the distortion/interaction-activation strain model, the potential energy $\mathbf{\Delta E}(\zeta)$ is decomposed into the distortion and the interaction energies, $\mathbf{\Delta E_{dist}}(\zeta)$ and $\mathbf{\Delta E_{int}}(\zeta)$, at each point ζ of the reaction coordinate, according to equation 1.

$$\mathbf{\Delta E}(\zeta) = \mathbf{\Delta E_{int}}(\zeta) + \mathbf{\Delta E_{dist}}(\zeta) \qquad (1)$$

The interaction energy is calculated as the difference between the energy of the complex geometry on the reaction coordinate and the sum of the energies of the distorted reactant fragments and accounts for the chemical interactions that occur between these fragments. The distortion or strain, on the other hand, corresponds to the energy required to deform the reactants from their equilibrium structure to the geometry adopted at point ζ of the reaction coordinate. $\mathbf{\Delta E_{dist}}(\zeta)$ can be further decomposed into the contribution of each of the reactants (in this case, the diene and the dienophile), according to equation 2, where $\mathbf{\Delta E_{dist\ Dph}}(\zeta)$ represents the distortion energy of the dienophile and $\mathbf{\Delta E_{dist\ Cp}}(\zeta)$, the distortion of the diene (cyclopentadiene).

$$\mathbf{\Delta E_{dist}}(\zeta) = \mathbf{\Delta E_{dist\ Dph}}(\zeta) + \mathbf{\Delta E_{dist\ Cp}}(\zeta) \qquad (2)$$

Fragment distortion and interaction energies at each point of the reaction coordinate were calculated using the autoDIAS set of scripts[15] at the SMD(toluene)-M06-2X/6-31+G* level. To build the distortion/interaction diagrams, the IRCs were projected onto the average distance of both

C-C forming bonds and energies were plotted against this critical geometrical parameter.

Energy Decomposition Analysis

The interaction energy can be further partitioned with an Energy Decomposition Analysis (EDA) scheme. In simple EDA, as performed by Multiwfn, ΔE_{int} is decomposed into terms associated with stabilizing orbital interactions (ΔE_{orb}) and generally destabilizing steric interactions (ΔE_{steric}), according to equation 3.

$$\Delta E_{int} = \Delta E_{orb} + \Delta E_{steric} \tag{3}$$

The orbital interaction energy is the stabilization energy arising from the orbital mixing of the fragments and accounts for the bond-pair formation, charge transfer and polarization. The steric interactions are generally destabilizing and include the quasiclassical electrostatic interactions between the unperturbed charge distributions of the fragments (ΔE_{elstat}), the destabilizing Pauli repulsion between closed-shell orbital (ΔE_{Pauli}) and the change of exchange-correlation energy in the complexation process (ΔE_{XC}). The ΔE_{orb} term can then be partitioned and analyzed by means of the ETS-NOCV (Extended Transition State-Natural Orbital for Chemical Valence),[16] which identifies the key molecular orbital interactions in the complex.

In this work, we selected the M06-2X/6-31+G* geometries with the same consistent average C-C forming bond distance of 2.3 Å and used Multiwfn to perform EDA-NOCV calculations at the M06-2X/6-31+G* level of theory on them.

Results

Table S1. Calculated activation and reaction free energies for the concerted mechanisms (in kcal/mol). Method A: M06-2X/6-31+G*, Method B: SMD(toluene)-M06-2X/6-31+G*, Method C: M06-2X/6-311++G**//M06-2X/6-31+G*, Method D: SMD(toluene)-M0-62X/6-311++G**//SMD(toluene)-M06-2X/6-31+G*.

Reaction	Method	$\Delta G^{\ddagger}$		$\Delta\Delta G^{\ddagger}$	ΔG		$\Delta\Delta G$
		endo	*exo*	*endo-exo*	*endo*	*exo*	*endo-exo*
4a + 2 → 5a	A	29.77	30.03	-0.26	-17.62	-17.97	0.35
	B	31.57	31.15	0.42	-15.58	-16.00	0.42
	C	29.99	30.26	-0.27	-15.93	-16.42	0.49
	D	31.77	31.73	0.04	-14.05	-14.46	0.41
4a + 2 → 6a	A	33.14	35.30	-2.16	-21.34	-21.73	0.39
	B	34.45	37.51	-3.06	-20.11	-19.83	-0.28
	C	33.87	35.77	-1.90	-19.35	-19.32	-0.03
	D	35.20	37.89	-2.69	-18.07	-17.61	-0.46
5a → 7a	A	49.28	52.51	-3.23	3.00	3.16	-0.16
	B	48.68	52.22	-3.54	2.15	2.70	-0.55
	C	48.73	51.89	-3.16	3.61	4.06	-0.45
	D	48.27	51.56	-3.29	3.01	3.61	-0.60
6a → 8a	A	56.64	54.91	1.73	10.50	10.17	0.33
	B	57.00	54.83	2.17	11.28	9.86	1.42
	C	55.93	53.32	2.61	10.66	10.00	0.66
	D	56.19	53.49	2.70	11.20	9.86	1.34
4b + 2 → 5b	A	27.14	27.74	-0.60	-21.11	-21.76	0.65
	B	28.13	29.44	-1.31	-18.74	-19.45	0.71
	C	27.19	27.71	-0.52	-19.69	-20.20	0.51
	D	28.43	29.58	-1.15	-17.26	-17.84	0.58
4b + 2 → 6b	A	30.64	32.72	-2.08	-26.32	-24.65	-1.67
	B	31.68	34.95	-3.27	-24.36	-23.14	-1.22
	C	30.82	33.09	-2.27	-24.23	-22.88	-1.35
	D	32.00	35.34	-3.34	-22.53	-21.22	-1.31
5b → 7b	A	50.30	52.62	-2.32	3.00	3.89	-0.89
	B	48.17	50.77	-2.59	1.70	2.46	-0.76
	C	49.72	51.86	-2.14	3.71	4.33	-0.62
	D	47.71	50.20	-2.49	2.47	3.12	-0.65
6b → 8b	A	59.40	55.11	4.29	12.38	9.57	2.81
	B	58.06	54.84	3.22	11.91	10.27	1.64
	C	58.22	54.17	4.05	12.01	9.64	2.37
	D	57.36	53.90	3.46	11.99	10.22	1.77
1a + 2 → 3a	A	27.54	26.74	-0.80	-9.86	-9.91	-0.05
	B	28.24	27.93	-0.31	-9.51	-9.27	0.24
	C	27.57	26.53	1.04	-8.34	-8.52	0.18
	D	28.38	27.80	0.58	-7.76	-7.90	0.14
1b + 2 → 3b	A	25.42	25.82	-0.40	-12.30	-12.69	0.39
	B	26.14	27.00	-0.86	-11.01	-11.12	0.11
	C	25.47	25.86	-0.39	-10.70	-10.86	0.16
	D	26.30	27.13	-0.83	-9.52	-9.51	-0.01

Frontier Molecular Orbitals
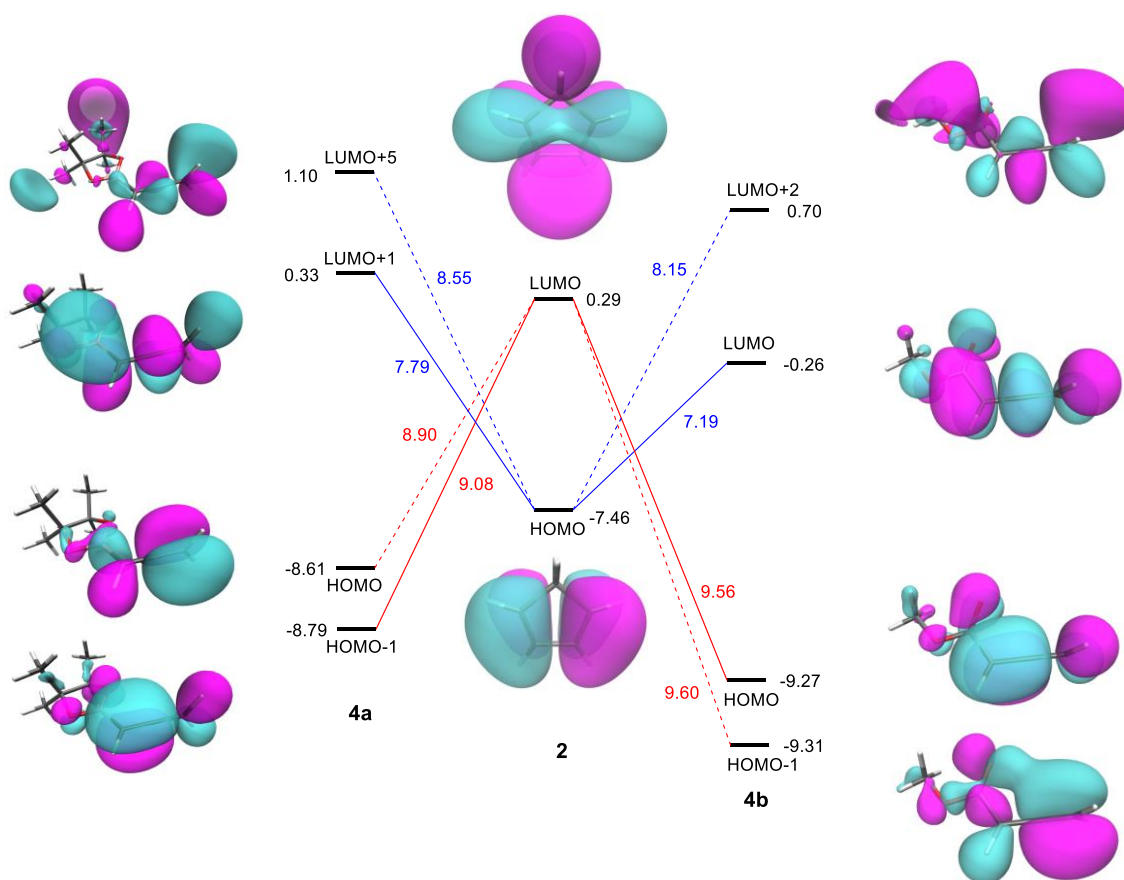
Figure S1. M06-2X/6-31+G* FMOs for the reactants. Energies in eV.

Contrary to previous results for **4a**, FMO analysis shows that the most reactive C-C double bond for compound **4b** is the internal bond, both for the nucleophilic (LUMO) and electrophilic (HOMO) attack. While the LUMO corresponding to the allene moiety for both compounds is mainly located on the internal double bond and the most electrophilic atom is the central carbon of the allene, the HOMO corresponds to the terminal bond for **4a** and to the internal bond for **4b**. However, the HOMO-1 of the carboxylic ester has a very similar energy to that of the HOMO ($\Delta\varepsilon$ = 0.04 eV) and is mainly located on the terminal bond. The HOMO-1 of the boronic ester **4a**, in contrast, is located on the internal bond and presents a bigger energy difference relative to the HOMO ($\Delta\varepsilon$ = 0.18 eV). In any case, the dominant interaction is that between the HOMO of the diene and the LUMO of the allene group for both dienophiles (normal electron demand DA reaction). Also, FMO energies are lower for **4b**, which gives lower a $HOMO_{diene}$-$LUMO_{dienophile}$ gap and is in line with its higher reactivity as a dienophile.

It is important to mention that the LUMO (not shown) computed at the M06-2X/6-31+G* level of theory for **4a** is mainly localized on the B atom, and would not be involved in the studied Diels-Alder reaction. Therefore, the lowest lying vacant orbital that could interact with the diene is the

LUMO+1, shown in Figure S1. For the DA reactions with the terminal double bond of the allenes, the unoccupied orbitals interacting with the HOMO of **2** must be localized around the terminal double bond, with a planar node between the two involved carbons. Furthermore, this orbital must have a planar node in the plane of the terminal hydrogens of the allene. The orbitals with the most adecquate shapes (i.e. that would lead to highest overlap for the formation of **6**) are the LUMO+5 for **4a** and LUMO+2 for **4b**. Normal electron demand energy gaps for the formation of **6a** and **6b** then must be calculated with the LUMO+5 and LUMO+2 for substrates **4a** and **4b**, respectively.
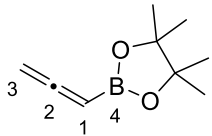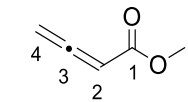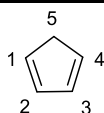
For the inverse electron demand DA reactions, the shapes of high energy occupied MOs must be analyzed. For the formation of **5**, the bonding π orbital that interacts with the LUMO of **2** must be localized on the internal double bond, with a planar node on the plane formed by the H-C-B atoms (or H-C-C=O atoms). Inverse electron demand (IED) DAs that lead to **5** proceed with the HOMO-1 of **4a** and the HOMO of **4b**. For the formation of **6**, a MO localized on the internal double bond, with a planar node on the plane of the terminal hydrogens must be involved. Such occupied MOs are the HOMO for **4a** and the HOMO-1 for **4b**.

Reactivity Indices

Table S2. M06-2X/6-31+G* calculated global reactivity indices, computed using the HOMO and the LUMO+1 for **4a** and the HOMO and LUMO for **4b**

	Chemical hardness (η) (au)	*Electronic chemical potential (μ) (au)*	*Global electrophilicity (ω) (eV)*	*ΔN_{max} (eV)*	*Nucleophilicity (N) (eV)*
4a	0.33	-0.15	0.96	1.36	2.12
4b	0.33	-0.18	1.26	1.58	1.46
2	0.29	-0.13	0.83	1.02	3.27

Table S3. M06-2X/6-31+G* calculated local reactivity indices

|	Atom number	Atom type	P_k^+	P_k^-	ω_k	N_k
	1	C	3.09	-0.04	**2.96**	-0.09
	2	C	-1.81	0.16	-1.74	0.34
	3	C	-1.67	0.83	-1.60	**1.77**
	4	B	2.25	0.07	2.16	0.14
	2	C	0.18	0.73	0.23	**1.07**
	3	C	0.39	0.29	**0.49**	0.42
	4	C	-0.08	-0.11	-0.10	-0.17
	1	C	0.23	-0.11	0.29	-0.17
	1	C	0.44	0.54	**0.36**	**1.76**
	2	C	0.12	0.05	0.10	0.15
	5	C	-0.18	-0.12	-0.15	-0.39
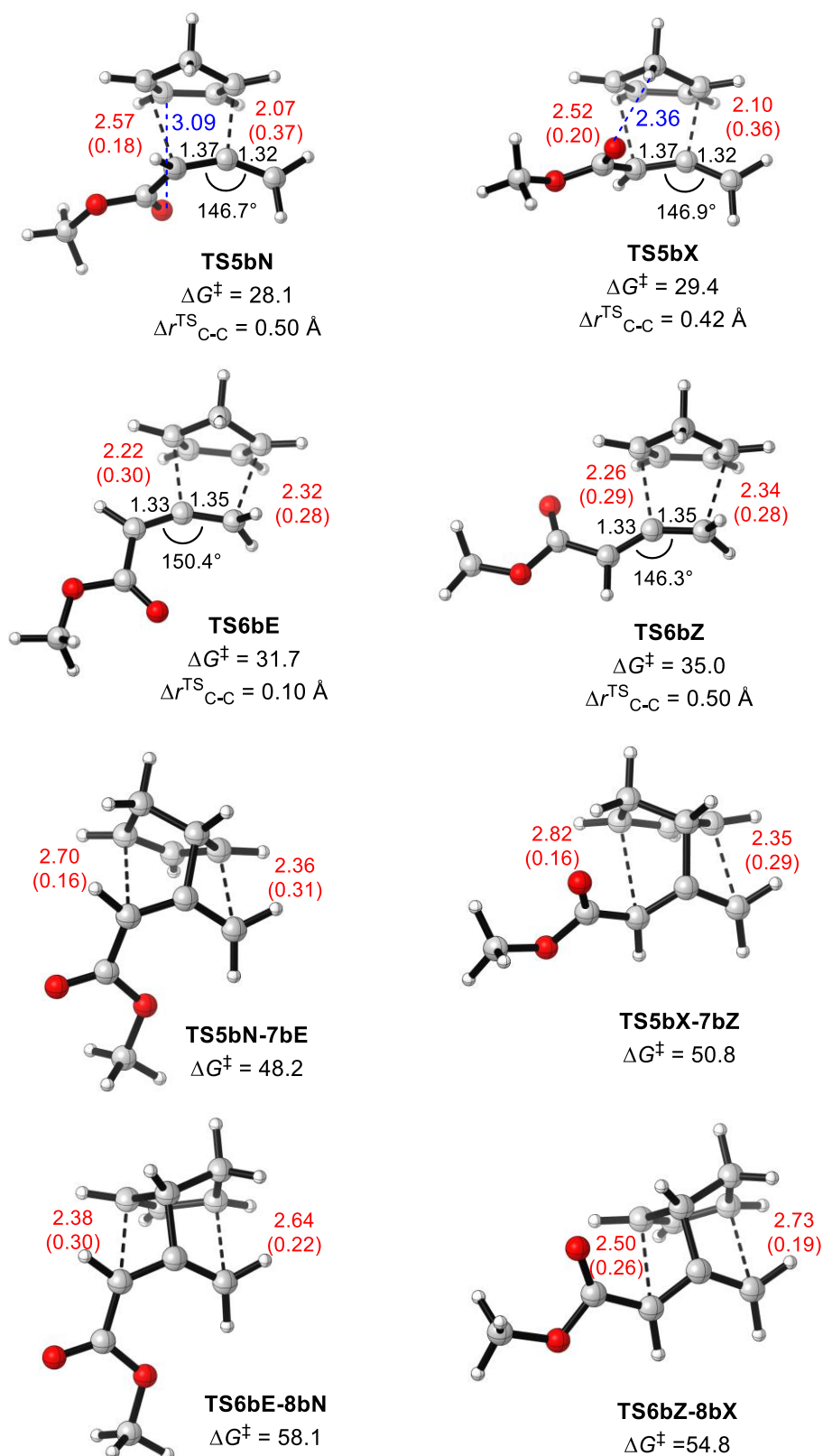
Figure S2. SMD(toluene)-M06-2X/6-31+G* optimized geometries of the transition states for the concerted mechanisms of the reaction between methyl 2,3-butadienoate (**4b**) and cyclopentadiene (**2**). Distances in Å, Wiberg indices between parentheses and energies in kcal/mol.
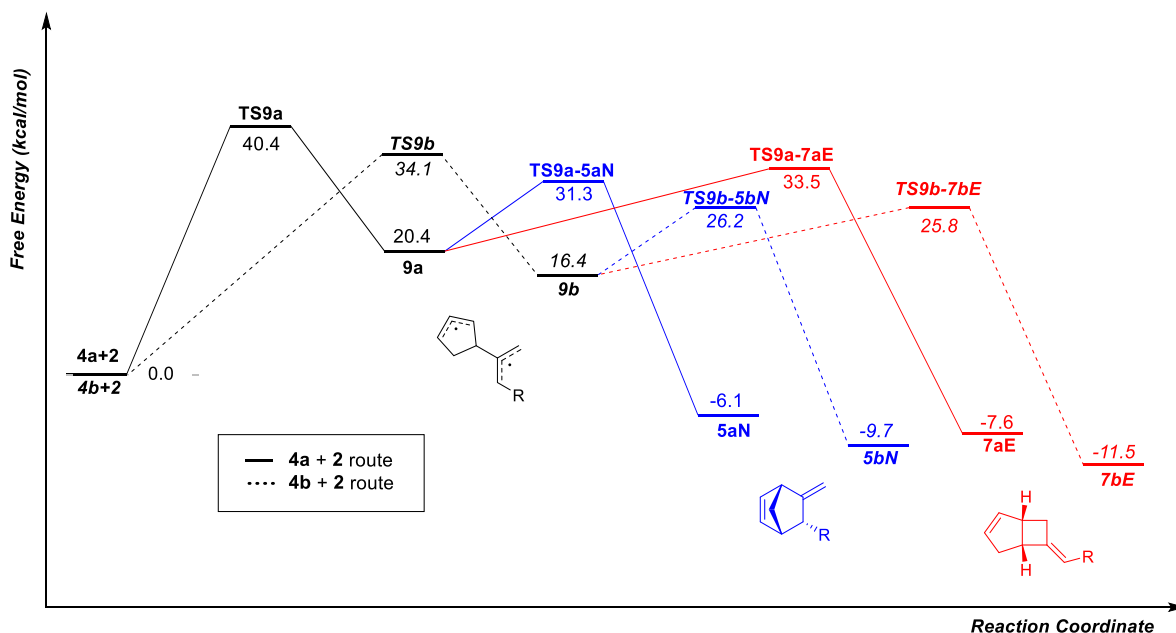
Stepwise Radical Mechanism

The competitive stepwise radical mechanism for the reaction between **4b** and **2** was modeled and the results were compared with those previously obtained for **4a**. We were able to locate the structures that lead to the formation of **5b** and **7b** *via* the 1,4-diradical intermediate **9b** (Scheme S1). For both dienophiles, the radical mechanism is disfavored (Figure S3) because formation of intermediate **9** is highly endergonic and the activation barrier is higher than that of the concerted DA cycloaddition leading to **5**. The difference between the activation energies is, however, lower for **4b** ($\Delta\Delta G^{\ddagger} \sim 2$ kcal/mol) than for **4a** ($\Delta\Delta G^{\ddagger} \sim 5$ kcal/mol).
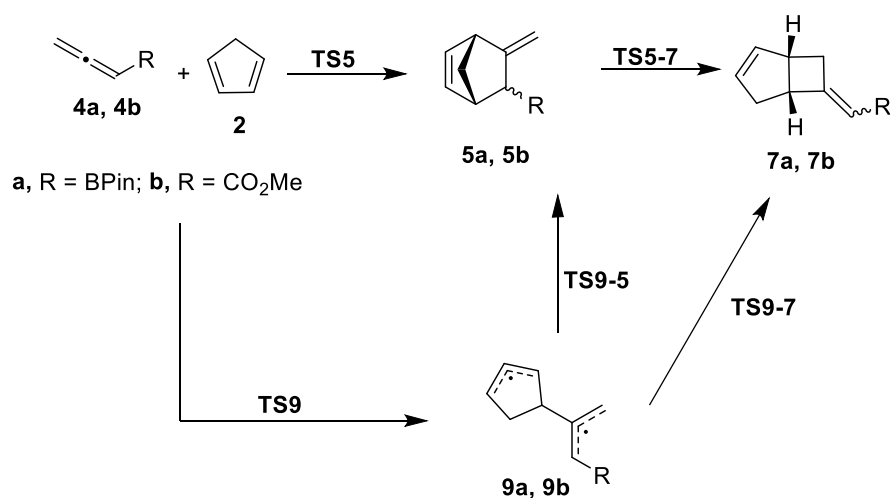
Scheme S1. Concerted and stepwise radical mechanisms for the formation of **5a, 5b** and **7a, 7b** from **4a** and **4b** with **2**.

Table S4. Calculated electronic and free energies (in kcal/mol) relative to starting materials and estimated value for $<S^2>$ before and after annihilation of the first spin contaminant at (U)B3LYP/6-31G* for the structures involved in the stepwise radical mechanism and in the concerted mechanism of the reactions between **4b** and **2**.

Structure	ΔE (SCF)	ΔG	$<S^2>$ (after annihilation)
TS5bN	17.9	32.2	0.00 (0.00)
TS5bX	17.2	31.81	0.00 (0.00)
TS9b (X)	20.1	34.1	0.00 (0.00)
9b	3.1	16.4	1.02 (0.63)
TS9b-5bN	10.1	26.2	0.40 (0.31)
TS9b-5bX	13.9	29.6	0.49 (0.36)
5bN	-28.8	-9.7	0.00 (0.00)
5bX	-29.5	-10.2	0.00 (0.00)
TS9b-7bE	10.4	25.8	0.42 (0.05)
TS9b-7bZ	15.6	31.0	0.30 (0.24)
7bE	-29.1	-11.5	0.00 (0.00)
7bZ	-29.1	-11.4	0.00 (0.00)

Figure S3. UB3LYP/6-31G* Reaction coordinate for the stepwise radical mechanism of the reactions of **4a** and **4b** with **2** with free energies in the gas phase (kcal/mol).

Distortion/Interaction Energies at the TSs

Table S5. Calculated distortion and interaction energies (in kcal/mol) at the TSs for the Diels-Alder reactions under study. Method A: M06-2X/6-31+G*, Method B: SMD(toluene)-M06-2X/6-31+G*.

Reaction	Method	Isomer	$\Delta E^{\ddagger}$	$\Delta E^{\ddagger}_{int}$	$\Delta E^{\ddagger}_{dist}$	$\Delta E^{\ddagger}_{dist\ Cp}$	$\Delta E^{\ddagger}_{dist\ Dph}$
4a + 2 → 5a	A	*endo*	15.0	-11.5	26.6	13.5	13.0
		exo	15.3	-10.8	26.1	13.1	13.0
	B	*endo*	16.9	-9.9	26.7	13.5	13.3
		exo	17.2	-9.3	26.6	13.2	13.4
4a + 2 → 6a	A	*E*	19.3	-6.5	25.8	13.6	12.1
		Z	20.8	-8.3	29.2	13.2	15.9
	B	*E*	20.6	-5.6	26.2	13.8	12.4
		Z	22.8	-6.7	29.5	13.4	16.1
4b + 2 → 5b	A	*endo*	12.1	-12.5	24.6	11.1	13.5
		exo	12.5	-12.3	24.8	11.2	13.7
	B	*endo*	13.7	-11.0	24.8	10.9	13.9
		exo	14.5	-10.8	25.3	11.1	14.3
4b + 2 → 6b	A	*E*	15.9	-7.4	23.3	12.4	10.9
		Z	17.8	-9.4	27.2	11.9	15.4
	B	*E*	17.2	-6.6	23.8	12.6	11.2
		Z	20.3	-7.3	27.7	12.0	15.7
1a + 2 → 3a	A	*endo*	12.2	-11.0	23.2	16.2	7.0
		exo	11.8	-10.5	22.2	15.4	6.8
	B	*endo*	13.4	-10.0	23.3	16.2	7.1
		exo	13.0	-9.5	22.6	15.4	7.2
1b + 2 → 3b	A	*endo*	9.9	-12.5	22.4	14.6	7.8
		exo	10.5	-12.1	22.6	14.4	8.2
	B	*endo*	11.0	-11.5	22.5	14.5	8.0
		exo	11.9	-11.1	23.0	14.5	8.5

Distortion/Interaction Energies at a Consistent Average Distance of 2.3 Å

Table S6. Calculated distortion and interaction energies (in kcal/mol) at the geometries with a consistent average distance of 2.3 Å for the Diels-Alder reactions under study. Method A: M06-2X/6-31+G*, Method B: SMD(toluene)-M06-2X/6-31+G*.

Reaction	Method	Isomer	ΔE	ΔE_{int}	ΔE_{dist}	$\Delta E_{dist\ Cp}$	$\Delta E_{dist\ Dph}$
4a + 2 → 5a	A	*endo*	14.8	-7.6	22.4	11.2	11.2
		exo	15.1	-6.8	21.9	10.7	11.2
	B	*endo*	16.7	-5.9	22.6	11.1	11.4
		exo	17.0	-5.3	22.3	10.8	11.5
4a + 2 → 6a	A	*E*	19.0	-2.1	21.2	11.1	10.1
		Z	20.6	-4.2	24.8	10.9	14.0
	B	*E*	20.4	-1.2	21.5	11.2	10.4
		Z	22.6	-2.5	25.1	11.0	14.2
4b + 2 → 5b	A	*endo*	12.1	-12.5	24.6	11.1	13.5
		exo	12.5	-12.3	24.8	11.2	13.7
	B	*endo*	13.7	-11.0	24.8	10.9	13.9
		exo	14.5	-10.8	25.3	11.1	14.3
4b + 2 → 6b	A	*E*	15.9	-7.4	23.3	12.4	10.9
		Z	17.8	-9.4	27.2	11.9	15.4
	B	*E*	17.2	-6.6	23.8	12.6	11.2
		Z	20.3	-7.3	27.7	12.0	15.7
1a + 2 → 3a	A	*endo*	12.0	-6.3	18.3	13.2	5.1
		exo	11.5	-6.0	17.5	12.5	5.1
	B	*endo*	13.2	-5.3	18.4	13.2	5.3
		exo	12.8	-5.0	17.8	12.5	5.4
1b + 2 → 3b	A	*endo*	9.7	-7.9	17.6	11.8	5.8
		exo	10.3	-7.5	17.8	11.6	6.2
	B	*endo*	10.8	-6.9	17.7	11.7	6.0
		exo	11.7	-6.6	18.3	11.8	6.6

Tables S5 and S6 show that the calculated distortion and interaction energies at the TSs and at the geometries with a consistent average distance of 2.3 Å are different. Since the former sometimes conduct to misleading conclusions due to the different positions of the TSs in the reaction coordinate, analysis along the entire reaction coordinate (or at a consistent point near the TS) is discussed herein.
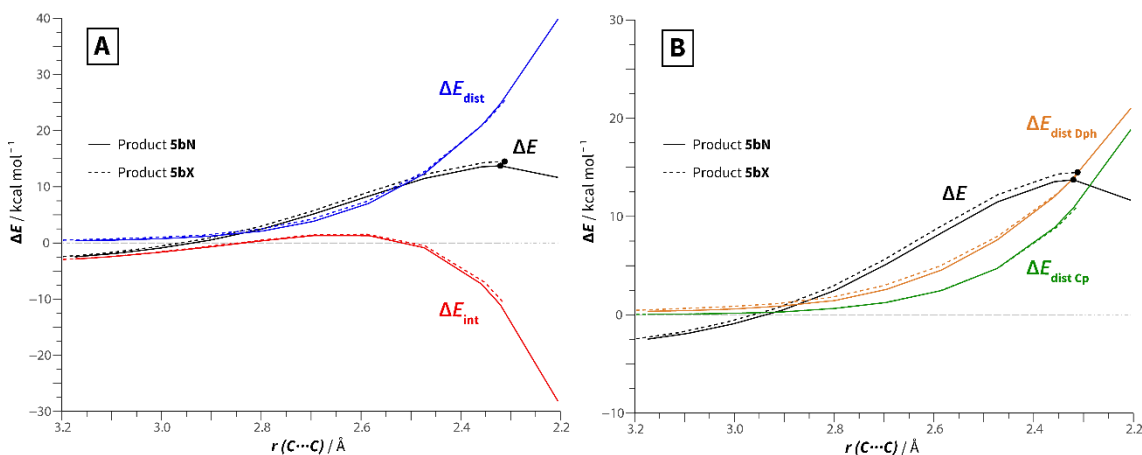
Distortion/Interaction Diagrams

Following are the comparative distortion/interaction diagrams not shown in the manuscript. In all cases keys are: (A) Total (black), interaction (red) and total distortion (blue) energies. (B) Total (black), dienophile distortion (orange) and cyclopentadiene distortion (green) energies. Energy values projected onto the average distance of the two forming C-C bonds. Data was computed at the SMD(toluene)-M06-2X/6-31+G* level of theory.

Figures S4, S5, S6 and S7 show the distortion/interaction diagrams comparing the formation of *endo* and *exo* adducts with each dienophile. In all cases, low to null selectivities are observed due to very low energy differences. Because of the small variations in electronic energy, the *endo/exo* selectivity cannot be clearly explained by this approach. However, slight differences in the interaction energies could be the dominant factor for the observed selectivities.
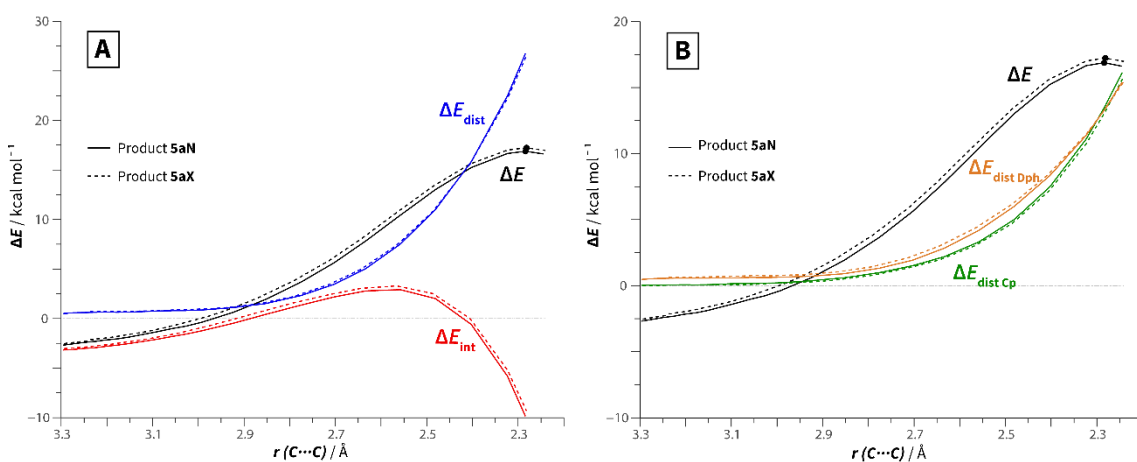
Figure S4. Comparative distortion/interaction diagrams for the formation of **5aN** and **5aX**.

Figure S5. Comparative distortion/interaction diagrams for the formation of **5bN** and **5bX**.
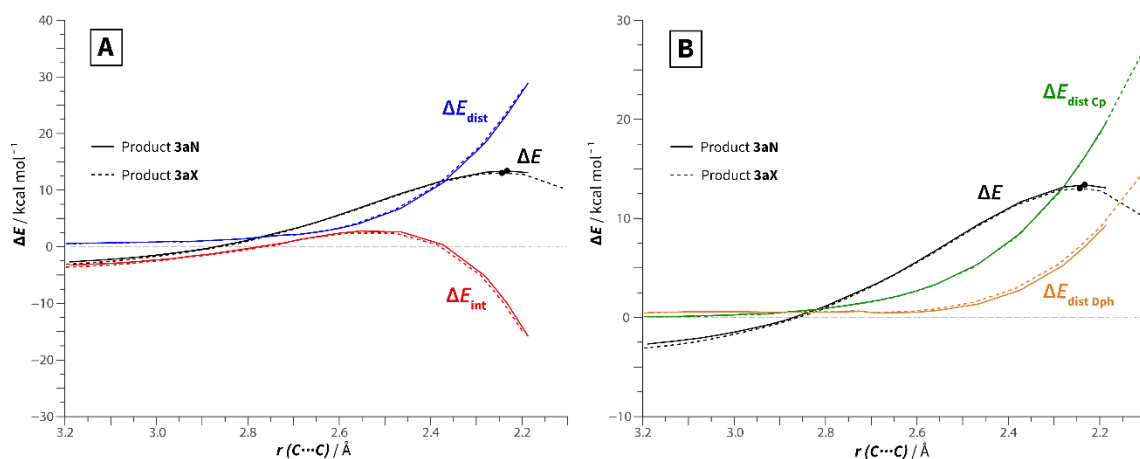
Figure S6. Comparative distortion/interaction diagrams for the formation of **3aN** and **3aX**.
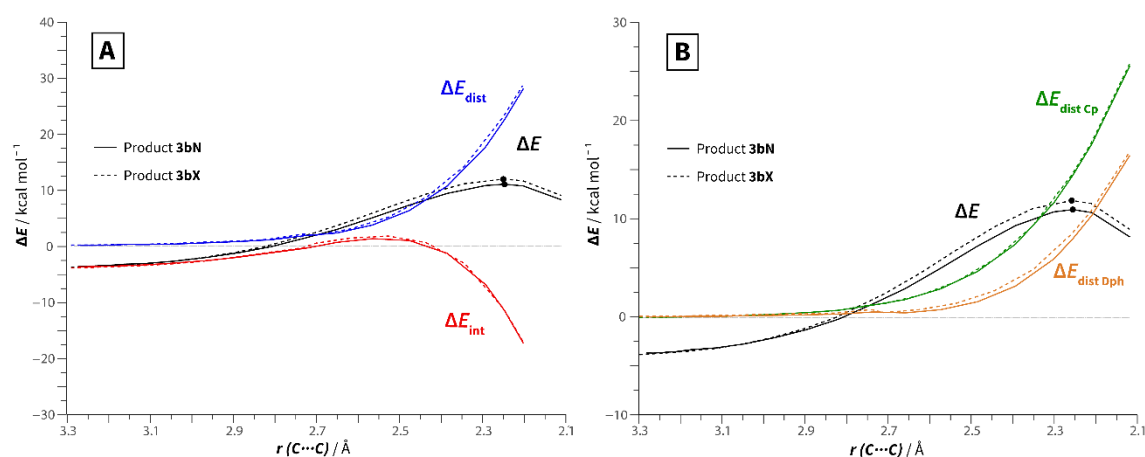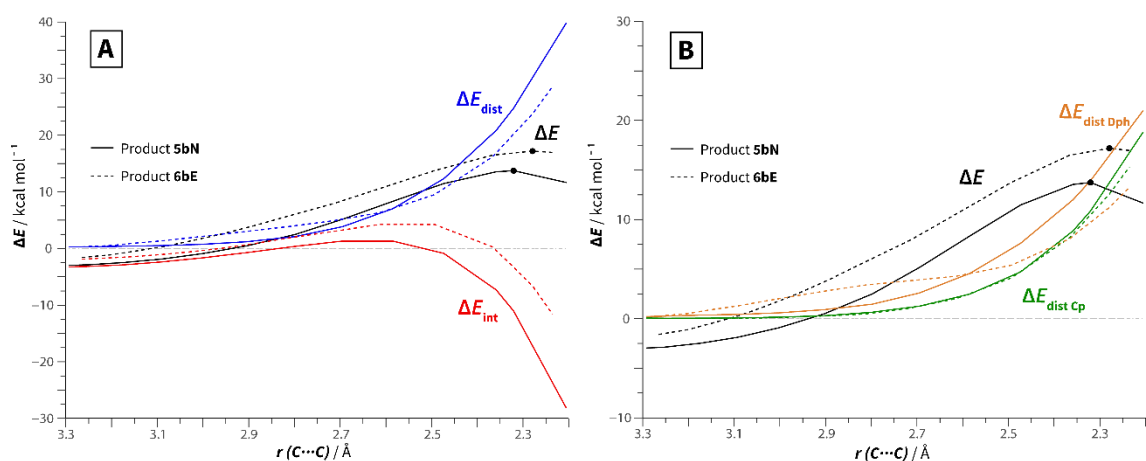

Figure S7. Comparative distortion/interaction diagrams for the formation of **3bN** and **3bX**.

Figure S8 shows the D/I diagrams for the formation of **5aX** and **6aZ**. As was found for the *endo/E* modes of cycloaddition, the dominant factor in determining the formation of **5aX** over **6aZ** is the interaction energy. Even though the distortion also favors the formation of **5aX**, the contribution of the interaction is greater. If we compare the geometries of the pertinent TSs, we find that the C-C-C bond angle is approximately the same for both geometries and this is related to the larger strain observed for **6Z** (in contrast to the smaller strain for **6E**). Therefore, we can conclude that in these processes, the strain is primarily related to the distortion of the C-C-C bond angle of the allene moiety.
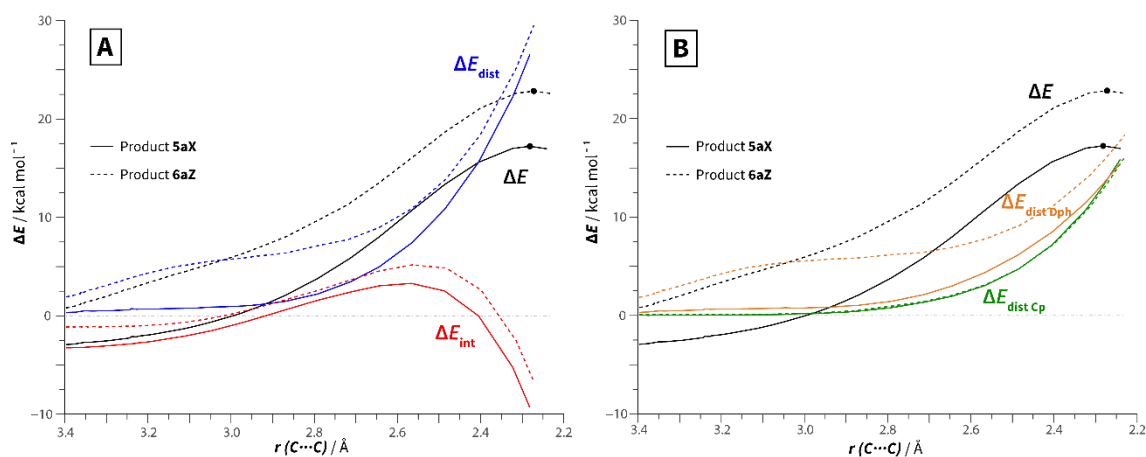
Figure S8. Comparative distortion/interaction diagrams for the formation of **5aX** and **6aZ**.

Figures S9 and S10 compare the formation of products **5b** and **6b**. Analysis of the plots allows us to arrive to the same conclusions as with the DA reactions of **4a**.
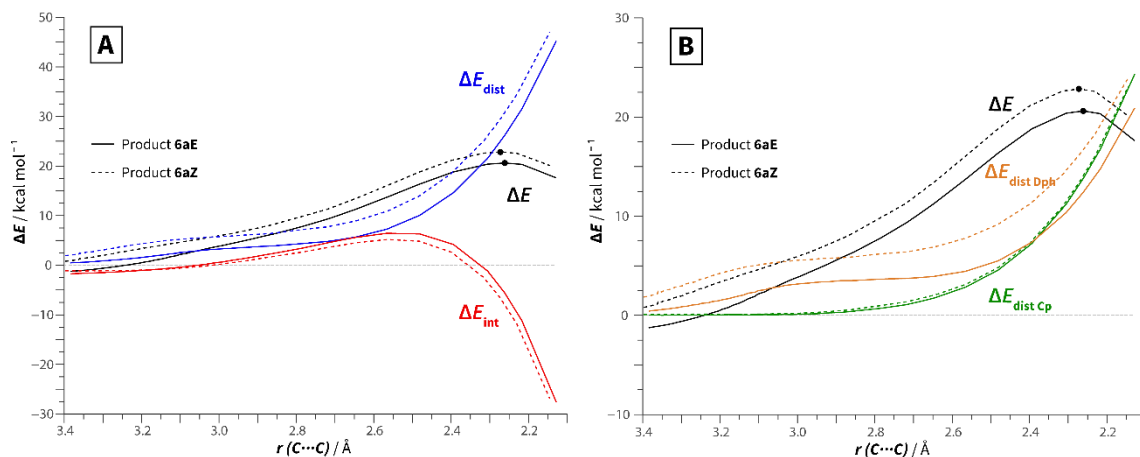

Figure S9. Comparative distortion/interaction diagrams for the formation of **5bN** and **6bE**.
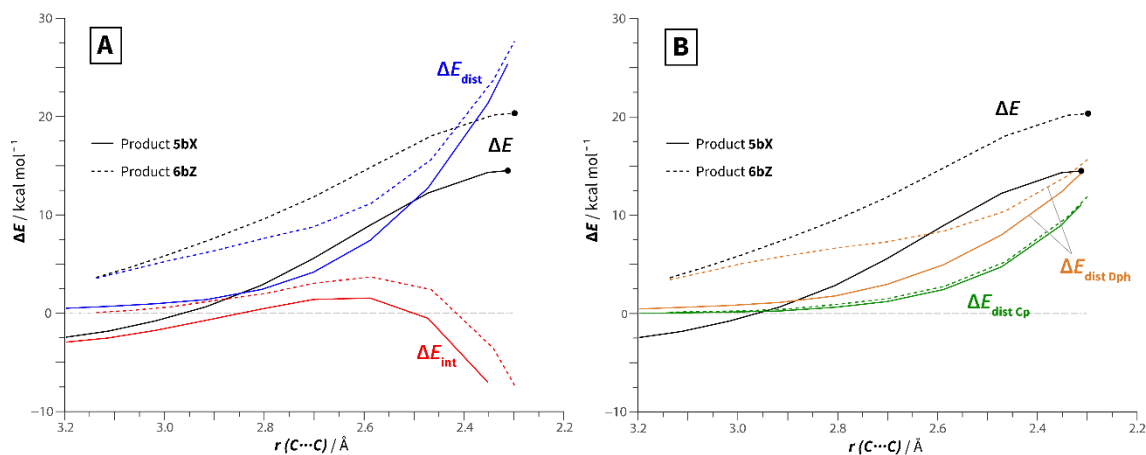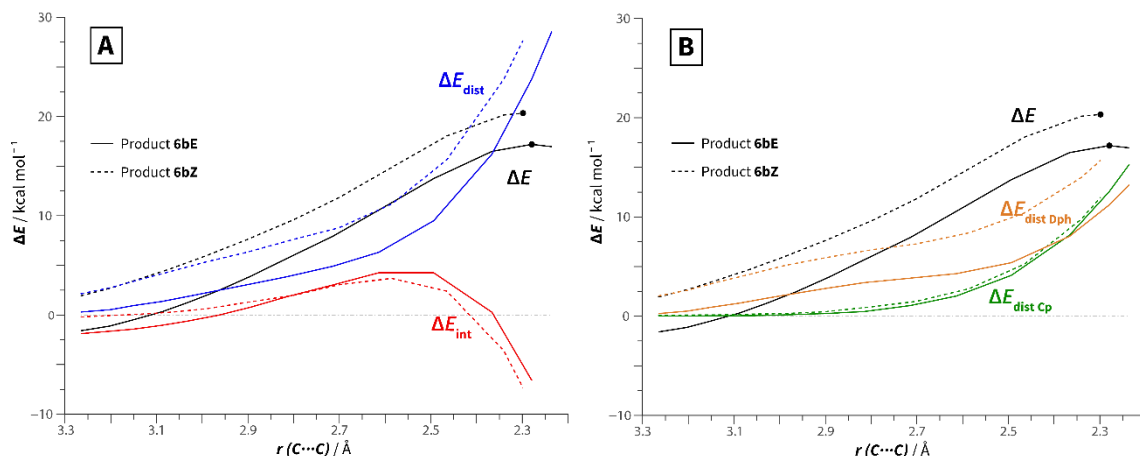

Figure S10. Comparative distortion/interaction diagrams for the formation of **5bX** and **6bZ**.

Figures S11 and S12 show the D/I diagrams for the formation of **6E** and **6Z**, for dienophiles **4a** and **4b**, respectively. For both substrates, we find that the distortion is larger for **6Z** (which is in agreement with the smaller C-C-C bond angle observed at the TSs) but the interaction is stronger. The contribution of the strain is more significant and this leads to higher activation barriers for **6Z**.
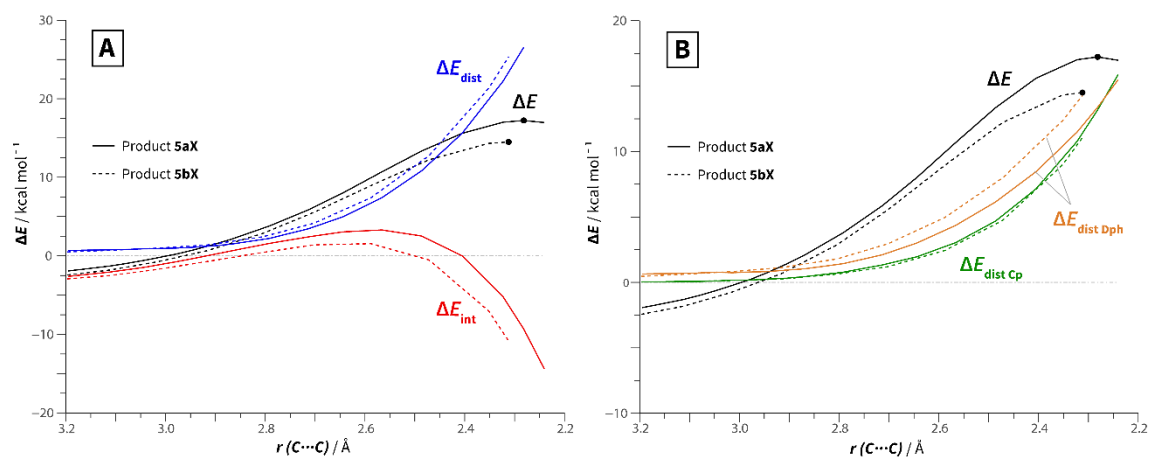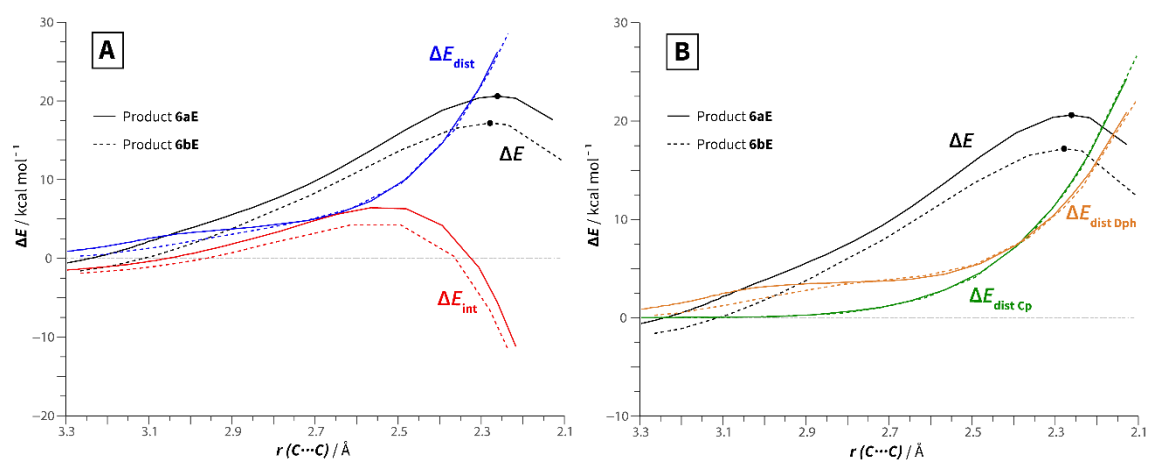

Figure S11. Comparative distortion/interaction diagrams for the formation of **6aE** and **6aZ**.

Figure S12. Comparative distortion/interaction diagrams for the formation of **6bE** and **6bZ**.
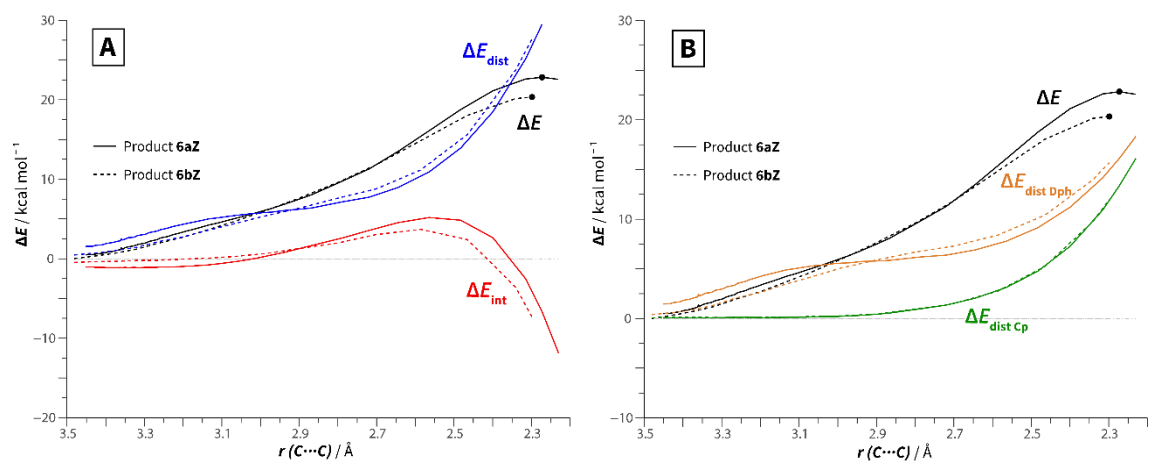
Figures S13, S14 and S15 compare the behavior of dienophiles **4a** and **4b** in the formation of products **5X**, **6E** and **6Z**, respectively. In all cases we find that the factor that determines the higher reactivity (lower activation barriers) of **4b** is the interaction. The contribution of the distortion is small (in the case of **5X** and **6Z** it favors the reactions of **4a**) and the observed difference depends solely on the strain of the dienophile.

Figure S13. Comparative distortion/interaction diagrams for the formation of **5aX** and **5bX**.
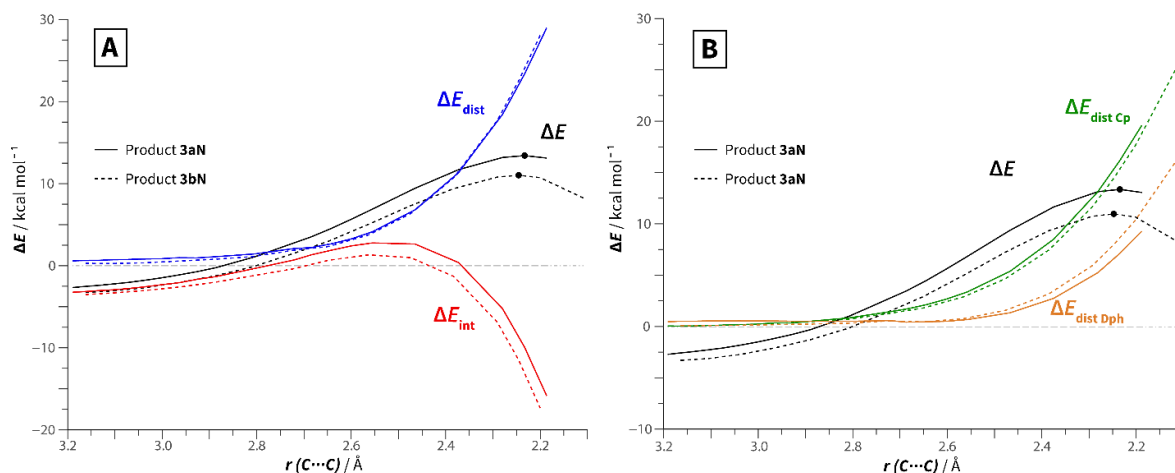

Figure S14. Comparative distortion/interaction diagrams for the formation of **6aE** and **6bE**.
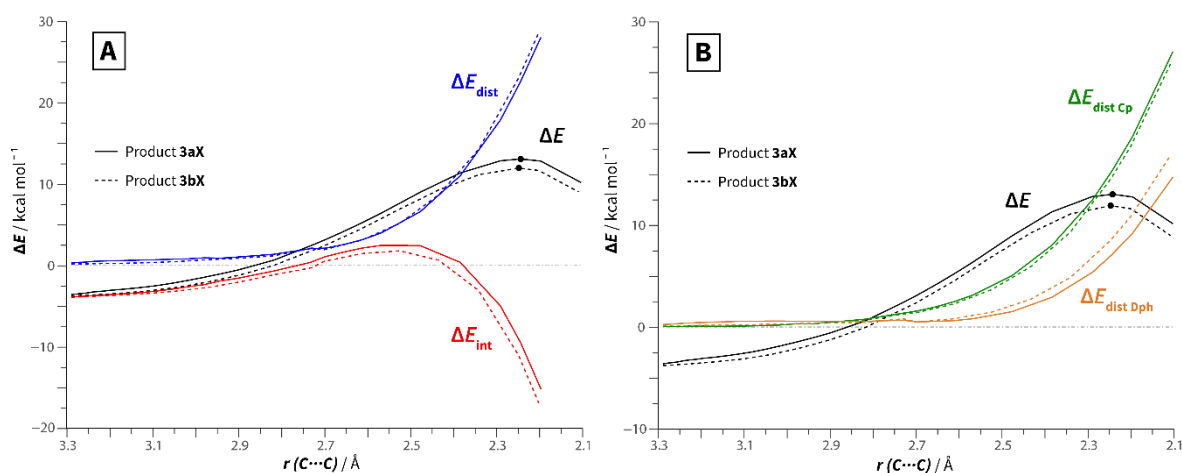

Figure S15. Comparative distortion/interaction diagrams for the formation of **6aZ** and **6bZ**.

Figures S16 and S17 compare the behavior of dienohpiles **1a** and **1b** in the formation of products **3N** and **3X**, respectively. Higher reactivity (lower reaction barrier) for **1b** can be explained by lower interaction energies along the reaction coordinate.
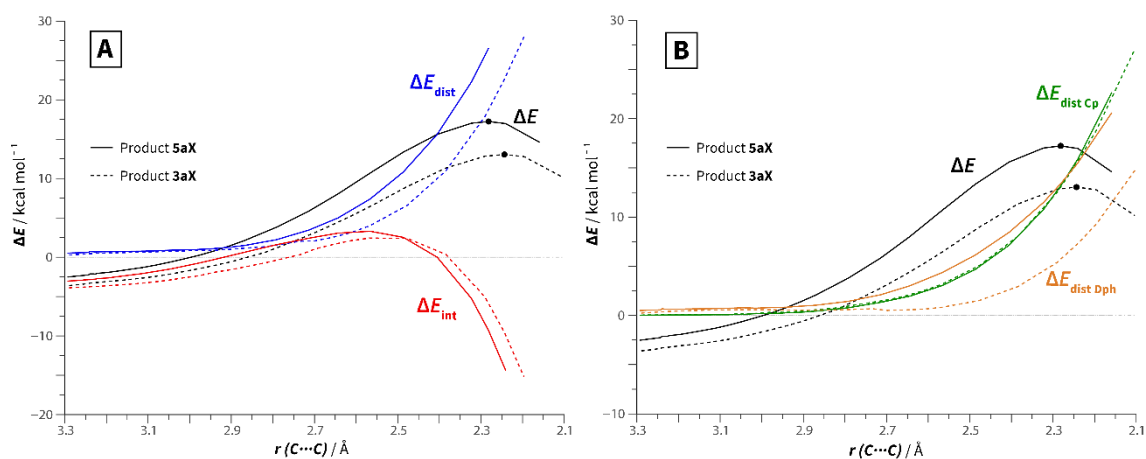

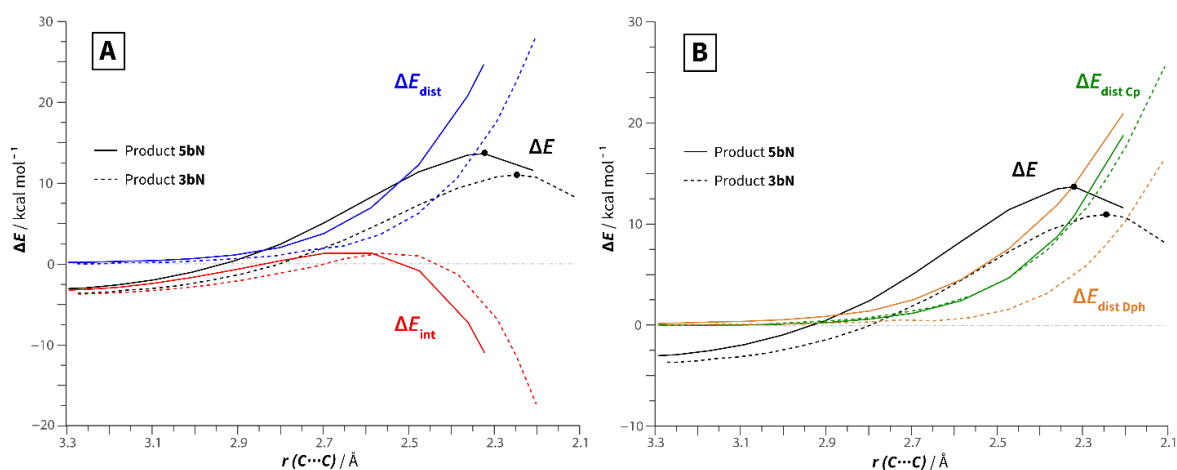**Figure S16.** Comparative distortion/interaction diagrams of the formation of **3aN** and **3bN**.

Figure S17. Comparative distortion/interaction diagrams of the formation of **3aX** and **3bX**.

Figure S18 shows the D/I diagrams for the formation of **5aX** and **3aX**. The same trends that were found for the *endo* reaction channels are observed.
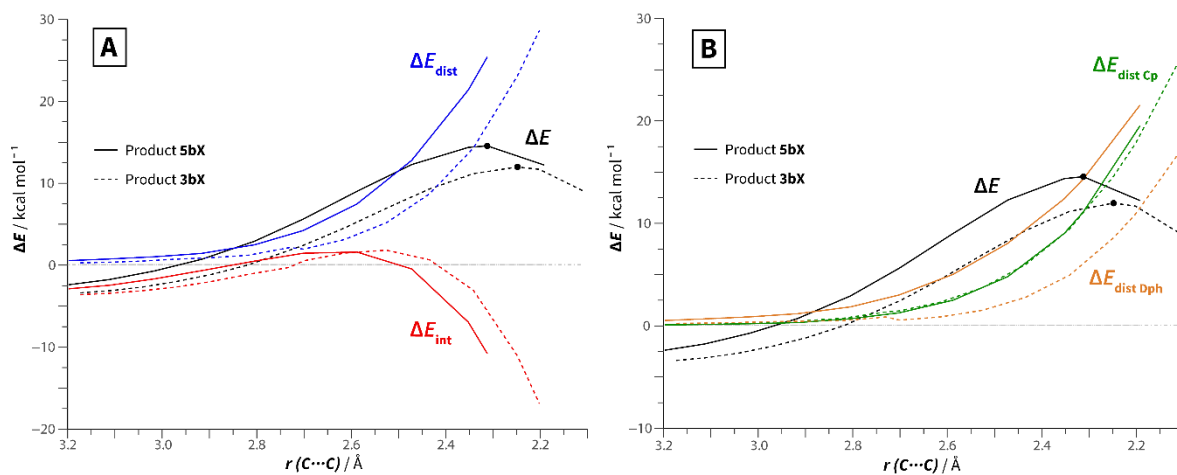
Figure S18. Comparative distortion/interaction diagrams for the formation of **5aX** and **3aX**.

Figures S19-S20 show the D/I diagrams for the formation of **5b** and **3b**, *endo* and *exo*. Results are similar to those of **5a** and **3a**.


**Figure S19.** Comparative distortion/interaction diagrams of the formation of **5bN** and **3bN**.

Figure S20. Comparative distortion/interaction diagrams of the formation of **5bX** and **3bX**.

EDA-NOCV calculations

Figures S21-23 show the relationship between the interaction energy and the terms computed by EDA, i.e., the orbital and the steric interaction energies. From Figure S21 we can conclude that there is a direct relationship between ΔE_{int} and ΔE_{orb}. If we analyze only the reactions of allenes **4a** and **4b** (Figure S22), we can find a very strong correlation between the two energies. On the contrary, the correlation between ΔE_{int} and ΔE_{steric} is very weak (Figure S23). This allows us to conclude that the orbital interaction energy is controlling the total interaction in the studied systems, mainly in the case of allenyl substrates.
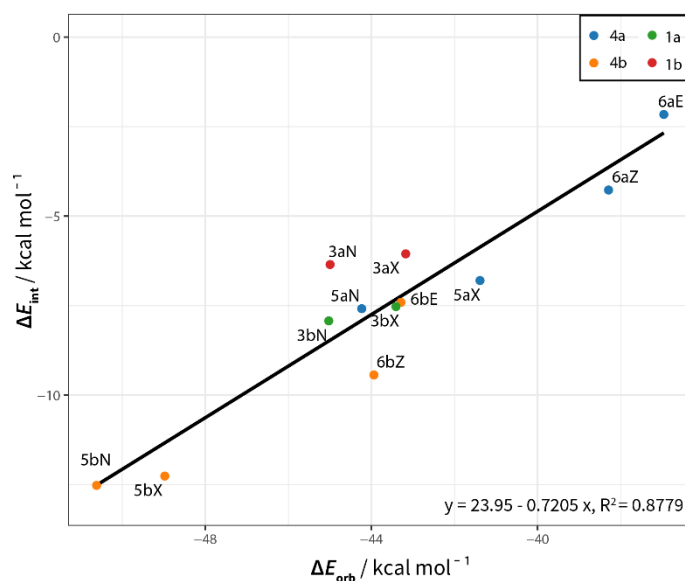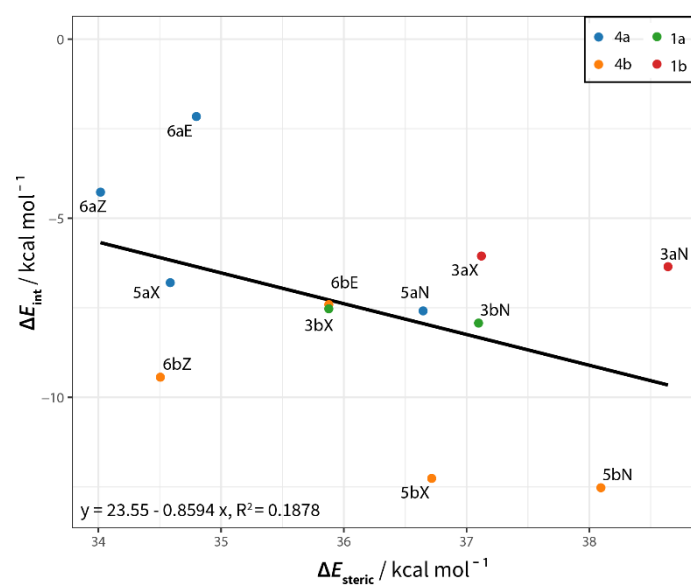

Figure S21. Plot of the interaction energies (ΔE_{int}) versus the orbital interaction energy (ΔE_{orb}) for the studied DA reactions. Data computed at M06-2X/6-31+G* on geometries with a consistent average C-C bond forming distance of 2.3 Å.
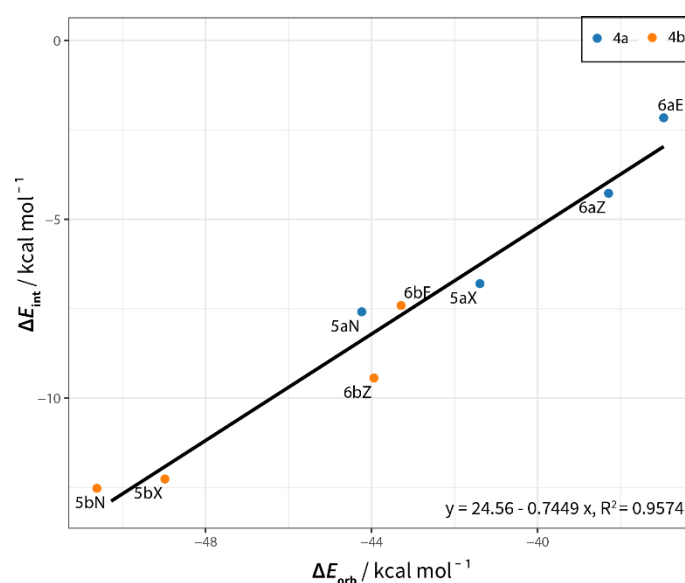
Figure S22. Plot of the interaction energies (ΔE_{int}) versus the orbital interaction energy (ΔE_{orb}) for the DA reactions of **4a** and **4b** with **2**. Data computed at M06-2X/6-31+G* on geometries with a

consistent average C-C bond forming distance of 2.3 Å.

Figure S23. Plot of the interaction energies (ΔE_{int}) versus the steric interaction energy (ΔE_{steric}) for the studied DA reactions. Data computed at M06-2X/6-31+G* on geometries with a consistent average C-C bond forming distance of 2.3 Å.

Table S7. Computed NOCV energies for key interactions and sum of all NOCV pair energies at the M06-2X/6-31+G* level of theory. Energies in kcal/mol.

Reaction	Isomer	$\Delta E(\rho_1)$	$\Delta E(\rho_2)$	Sum of all NOCV pairs
4a + 2 → 5a	*endo*	-37.6	-23.9	-67.4
	exo	-35.1	-23.0	-63.8
4a + 2 → 6a	E	-29.4	-24.1	-57.7
	Z	-31.4	-22.8	-59.4
4b + 2 → 5b	*endo*	-46.2	-24.2	-76.4
	exo	-44.4	-24.2	-75.0
4b + 2 → 6b	E	-36.2	-26.9	-67.6
	Z	-38.9	-23.8	-68.4

Table S8. Energies for the FMO interactions involved in the DA reactions between **4a**, **4b** and **2** computed at the M06-2X/6-31+G* level of theory. Energies in eV.

Reaction	ε_{HOMO}	ε_{LUMO}	NED gap	IED gap
4a + 2 → 5a	-8.79	0.33	7.79	9.08
4a + 2 → 6a	-8.61	1.10	8.55	8.90
4b + 2 → 5b	-9.27	-0.26	7.19	9.56
4b + 2 → 6b	-9.31	0.44	8.15	9.60

References

(1) Frisch, M. J.; Trucks, G. W.; Schlegel, H. B.; Scuseria, G. E.; Robb, M. A.; Cheeseman, J. R.; Scalmani, G.; Barone, V.; Petersson, G. A.; Nakatsuji, H.; Li, X.; Caricato, M.; Marenich, A.; Bloino, J.; Janesko, B. G.; Gomperts, R.; Mennucci, B.; Hratchian, H. P.; Ortiz, J. V.; Izmaylov, A. F.; Sonnenberg, J. L.; Williams-Young, D.; Ding, F.; Lipparini, F.; Egidi, F.; Goings, J.; Peng, B.; Petrone, A.; Henderson, T.; Ranasinghe, D.; Zakrzewski, V. G.; Gao, J.; Rega, N.; Zheng, G.; Liang, W.; Hada, M.; Ehara, M.; Toyota, K.; Fukuda, R.; Hasegawa, J.; Ishida, M.; Nakajima, T.; Honda, Y.; Kitao, O.; Nakai, H.; Vreven, T.; Throssell, K.; Montgomery, J. A. Jr.; Peralta, J. E.; Ogliaro, F.; Bearpark, M.; Heyd, J. J.; Brothers, E.; Kudin, K. N.; Staroverov, V. N.; Keith, T.; Kobayashi, R.; Normand, J.; Raghavachari, K.; Rendell, A.; Burant, J. C.; Iyengar, S. S.; Tomasi, J.; Cossi, M.; Millam, J. M.; Klene, M.; Adamo, C.; Cammi, R.; Ochterski, J. W.; Martin, R. L.; Morokuma, K.; Farkas, O.; Foresman, J. B.; Fox, D. J. *Gaussian 09,* Revision C.01; Gaussian, Inc.: Wallingford CT, 2016.

(2) Legault, C. Y. *CYLview,* Ver. 1.0b; Université de Sherbrooke, 2009. http://www.cylview.org/

(3) Lu, T.; Chen, F. Multiwfn: A Multifunctional Wavefunction Analyzer. *J. Comput. Chem.* **2012**, *33*, 580–592.

(4) Humphrey, W.; Dalke, A.; Schulten, K. VMD – Visual Molecular Dynamics. *J. Mol. Graphics* **1996**, *14*, 33–38.

(5) Stone, J. An Efficient Library for Parallel Ray Tracing and Animation. Master's Thesis, Computer Science Department, University of Missouri-Rolla, 1998.

(6) *Hyperchem Professional Release 7.52*; Hypercube, Inc., 2005.

(7) Zhao, Y.; Truhlar, D. G. The M06 Suite of Density Functionals for Main Group Thermochemistry, Thermochemical Kinetics, Noncovalent Interactions, Excited States, and Transition Elements: Two New Functionals and Systematic Testing of Four M06-Class Functionals and 12 Other Functionals. *Theor. Chem. Acc.* **2008**, *120*, 215–241.

(8) Liu, F.; Paton, R. S.; Kim, S.; Liang, Y.; Houk, K. N. Diels–Alder Reactivities of Strained and Unstrained Cycloalkenes with Normal and Inverse-Electron-Demand Dienes: Activation Barriers and Distortion/Interaction Analysis. *J. Am. Chem. Soc.* **2013**, *135*, 15642–15649.

(9) Sakata, K.; Fujimoto, H. Roles of Lewis Acid Catalysts in Diels-Alder Reactions between Cyclopentadiene and Methyl Acrylate. *ChemistryOpen* **2020**, *9*, 662–666.

(10) Marenich, A. V.; Cramer, C. J.; Truhlar, D. G. Universal Solvation Model Based on Solute Electron Density and on a Continuum Model of the Solvent Defined by the Bulk Dielectric Constant and Atomic Surface Tensions. *J. Phys. Chem. B* **2009**, *113*, 6378–6396.

(11) Becke, A. D. Density-functional Thermochemistry. III. The Role of Exact Exchange. *J. Chem. Phys.* **1993**, *98*, 5648–5652.

(12) Becke, A. D. Density-Functional Exchange-Energy Approximation with Correct Asymptotic Behavior. *Phys. Rev. A* **1988**, *38*, 3098–3100.

(13) Domingo, L. R.; Ríos-Gutiérrez, M.; Pérez, P. Applications of the Conceptual Density Functional Theory Indices to Organic Chemistry Reactivity. *Molecules* **2016**, *21*, 748.

(14) Domingo, L. R.; Pérez, P.; Sáez, J. A. Understanding the Local Reactivity in Polar Organic Reactions through Electrophilic and Nucleophilic Parr Functions. *RSC Adv.* **2013**, *3*, 1486–1494.

(15) Svatunek, D.; Houk, K. N. AutoDIAS: A Python Tool for an Automated Distortion/Interaction Activation Strain Analysis. *J. Comput. Chem.* **2019**, *40*, 2509–2515.

(16) Mitoraj, M. P.; Michalak, A.; Ziegler, T. A Combined Charge and Energy Decomposition Scheme for Bond Analysis. *J. Chem. Theory Comput.* **2009**, *5*, 962–975.